

Fig. 1. Principle and design of mid-IR narrowband high-contrast-ratio GFRs. (a) Schematic diagram defining the orientation and polarization of incident light and the structural parameters of the GFR. TE, transverse electric. TM, transverse magnetic. (b) Incident mid-IR radiation gets reflected via two channels presented in the structure, Lorentzian narrow-linewidth guided resonance and broadband Fabry–Pérot (F–P) reflection. (c) Computed F–P reflectance spectra vs. thickness for a flat thin-film slab with an effective thickness  $t_{\text{slab}} = d_2 + d_1/2$  and refractive indices  $n_{\text{SiN}} = 2.02$  and  $n_{\text{SL}} = 1.47$  at normal incidence. Cutoff curves of the several lowest-order guided modes are combined with the reflectance contours for design of GFRs. (d) Calculated dispersion curves of the two fundamental guided modes,  $\text{TE}_0$  and  $\text{TM}_0$ , in a flat thin-film slab with  $t_{\text{slab}} = 730$  nm. Higher-order modes  $\text{TE}_1$  and  $\text{TM}_1$  have cutoff wavenumbers of 5984 and 6935  $\text{cm}^{-1}$ , respectively, and are beyond the frequency range here. The inset illustrates how to determine  $\Lambda$  for a given  $\nu_{\text{res}}$  based on a dispersion curve. (e) Analytically predicted  $\Lambda$  vs. resonance wavenumber (white dashes) near the C–H stretching region. FEM-computed reflectance maps for a physical structure with  $[\theta_1, \theta_2, f, d_2, d_1] = [55^\circ, 55^\circ, 0.35, 580 \text{ nm}, 300 \text{ nm}]$  (corresponding to  $t_{\text{slab}} = 730$  nm) are overlaid for comparison.

When illuminated by a broadband source, the coupling between the incident light and the periodic subwavelength structure may occur in two ways. (i) Incident light at  $\lambda$  couples to the discrete in-plane guided mode supported by the structure via  $\pm$  1st-order Bragg scattering described by the momentum-matching condition:

$$\mathbf{k}_{\text{mode}} = \hat{x} |\mathbf{k}_0| \sin \theta_i \pm \mathbf{G}_x \quad (1)$$

where  $\mathbf{k}_{\text{mode}}$  is the wavevector of a specific guided mode,  $\hat{x}$  is the unit vector in the  $x$  direction,  $\mathbf{k}_0$  is the wavevector for the incident light ( $|\mathbf{k}_0| = 2\pi/\lambda$ ),  $\theta_i$  is the angle of incidence ( $\theta_i = 0^\circ$  is chosen for single-peak resonance in the present work), and  $\mathbf{G}_x$  is the reciprocal lattice vector ( $|\mathbf{G}_x| = 2\pi/\Lambda$ ). The mechanism creates a sharp resonance peak in the spectra (resonant Wood’s anomalies) [45–47]. (ii) Incident light couples to the continuum broadband vertical Fabry–Pérot (F–P) microcavity [48], as illustrated in Fig. 1(b). Processes (i) and (ii) take place simultaneously, leading to a total reflectivity spectrum,  $R(\nu)$ , expressed as a phenomenological Fano interference model [45, 49] given as

$$R(\nu) = |r(\nu)|^2 = \left| a_c(\nu) + b_r e^{-i\phi} \frac{\Delta\nu/2}{i(\nu - \nu_{\text{res}}) + \Delta\nu/2} \right|^2 \quad (2)$$

where  $R(\nu)$  is an interference effect of the continuum direct contribution (with amplitude  $a_c$ ) and the discrete Lorentzian resonance (with amplitude  $b_r$ , resonance wavenumber  $\nu_{\text{res}}$ , and bandwidth  $\Delta\nu$ ) with a phase difference  $\phi$ . Within an appropriate spectral range, the slowly-varying continuum  $a_c(\nu)$  can be expressed approximately as  $a_c(\nu) = a_0 + a_1\nu + a_2\nu^2$ , where  $a_0$ ,  $a_1$ , and  $a_2$  are fit parameters. When  $\nu = \nu_{\text{res}}$ , the ratio of the power in the guided resonance to that in the continuum background is  $P_r/P_c = |b_r/a_c(\nu_{\text{res}})|^2$  [50]. A resonance spectrum with a symmetric lineshape occurs when the phase difference  $\phi = 0$  [49] or  $a_c = 0$  [45]. When  $|\nu - \nu_{\text{res}}| \gg \Delta\nu$ , the incident wave does not satisfy the momentum-matching condition and cannot be coupled into the guided mode. Thus, only the continuum F–P multiple reflections determine the background reflectance. When  $|\nu - \nu_{\text{res}}| \leq \Delta\nu$ , the reflected wave is the interference of the guided mode and F–P reflections, exhibiting an asymmetric Fano lineshape [45, 49]. The coherent interference between a discrete narrow-linewidth and broadband contributions originates from atomic physics [51], and has been observed in a variety of photonic/plasmonic micro- and nano-systems [43, 52–57].

A figure of merit for spectroscopic sensing, which depends on separating the peak reflectance of the resonance ( $R_{\text{peak}}$ ) from the continuum reflectance in the vicinity of the resonance ( $R_{\text{vicinity}}$ ), is proposed here as a contrast ratio ( $CR$ ):

$$CR = \frac{R_{\text{peak}}}{R_{\text{vicinity}}} \quad (3)$$

Ideally, a GFR for spectroscopy must have a high  $CR$  and therefore a low  $R_{\text{vicinity}}$ . Second, a guided resonance must occur at a targeted wavelength. Therefore, it is essential to assure that the in-plane guided mode is not cut off when layer thicknesses are optimized for low continuum reflectance. Here, based on these considerations we use an efficient analytical methodology in designing narrowband GFRs.

The  $\text{Si}_3\text{N}_4$  slab thickness determines both the broadband continuum F–P reflection and the guided mode dispersion  $k_{\text{mode}}(\nu)$ . By ignoring the periodically structured surface to a first approximation for GFRs with a narrow linewidth, the GFR structure becomes an equivalent flat thin-film slab of effective thickness  $t_{\text{slab}} = d_2 + d_1/2$ , whose F–P reflectivity ( $R_{\text{F-P}}$ ) and guided mode cutoffs can be computed separately using the propagation matrix method [58, 59] and dielectric waveguide theory [59], respectively (see Appendix A and B for the methods).

Figure 1(c) presents the analytically calculated  $R_{\text{F-P}}$  spectrum of the equivalent flat thin-film slab for normal incidence and cutoff wavenumber of several lowest-order guided modes as a function of  $t_{\text{slab}}$ . In our GFRs, fundamental guided modes  $\text{TE}_0$  and  $\text{TM}_0$  are employed for resonances in the C–H stretching region, and therefore this spectral range for a  $t_{\text{slab}}$  has to be above the cutoffs for  $\text{TE}_0$  and  $\text{TM}_0$  modes. Additionally, the higher-order modes are designed to be cut off in the C–H stretching region in order to display a single resonance peak [44]. Thus, the spectral range for a  $t_{\text{slab}}$  must be below the cutoffs for  $\text{TE}_1$  and  $\text{TM}_1$  modes. At the same time, high  $CR$  requires small  $R_{\text{vicinity}}$  near the spectral location of resonance, which suggests locating the C–H stretching region for a  $t_{\text{slab}}$  between two ridges of high  $R_{\text{F-P}}$  in Fig. 1(c). Here, we choose  $t_{\text{slab}} = 730$  nm (yellow dashed line in Fig. 1(c)) for low  $R_{\text{F-P}}$  around  $2800\text{--}3300$   $\text{cm}^{-1}$  and fundamental-mode ( $\text{TE}_0$  or  $\text{TM}_0$ ) operation. After engineering both broadband F–P reflection and guided mode cutoffs, the structure period  $\Lambda$  is determined analytically based on the momentum-matching condition (Eq. (1)) in order to locate resonances in the targeted spectral region. Predicting  $\Lambda$  for a given  $\nu_{\text{res}}$  using Eq. (1) requires knowing dispersion curves of  $k_{\text{mode}}(\nu)$ , which are plotted in Fig. 1(d) for  $\text{TE}_0$  and  $\text{TM}_0$  guided

modes (calculated with Eq. (9) and (10) in Appendix B). The dispersion curves start from the cutoff condition on the substrate light line ( $k_{\text{mode}} = k_0 n_{\text{SL}}$ ) and approach the slab light line ( $k_{\text{mode}} \rightarrow k_0 n_{\text{SiN}}$ ) for high-wavenumber limit. Normally-incident IR radiation above the air light line acquires a momentum of  $2\pi/\Lambda$  in the  $x$  direction and then couples to the guided mode dispersion  $k_{\text{mode}}(\nu)$  based on the momentum-matching condition  $|k_{\text{mode}}(\nu)| = k_{\text{mode}}(\nu) = 2\pi/\Lambda$ , which determines and predicts  $\Lambda$  for a given  $\nu_{\text{res}}$  (as illustrated in the inset of Fig. 1(d)). As shown in Fig. 1(e), the analytically predicted period  $\Lambda$  is plotted as a function of resonance wavenumber for TE and TM polarizations, showing good agreement with the reflectivity map computed with FEM (COMSOL Multiphysics) for a physical structure for comparison, where  $d_1$  is chosen to be 300 nm for a narrow resonance bandwidth of  $\sim 30 \text{ cm}^{-1}$  at  $2700\text{--}3200 \text{ cm}^{-1}$  [44]. To compare with the results of analytical predictions the same refractive indices ( $n_{\text{SiN}} = 2.02$  and  $n_{\text{SL}} = 1.47$ ) were used in the FEM computation in Fig. 1(e). FEM computation also verifies low continuum background that is predicted by the analytical approach in Fig. 1(c) in the vicinity of the C–H stretching region. Thus, we provide an analytical framework for design of high-efficiency narrowband GFRs.

## 2.2 Experimental realization and validation of large-area narrowband high-CR mid-IR GFRs

The dispersion diagram in Fig. 1(d) indicates that the spectral position of the resonance is sensitive to the angle of incidence based on Eq. (1). For example, Fig. 2 shows the effect of varying angle of incidence ( $\theta_i$ ) on the reflectance spectra of the GFR, indicating that off-normal incident light results in two reflectance peaks compared to the case at normal incidence. Therefore, our GFRs are designed for collimated normal incidence instead of tight focusing on a small area. This necessitates a practical constraint that the area of a resonator structure be large to collect enough light.

Based on these constraints and the desired spectral range of  $2700\text{--}3200 \text{ cm}^{-1}$  in mid-IR, we fabricated a group of (seven) large-area ( $>20 \times 20 \text{ mm}^2$ ) GFRs on a 4-inch soda lime glass substrate. First, a  $\text{Si}_3\text{N}_4$  thin film with a thickness of  $\sim 880 \text{ nm}$  was deposited on soda lime glass (Mark Optics) by plasma-enhanced chemical vapor deposition (Mesc Multiplex PECVD, STS) at a pressure of 900 mTorr, temperature of  $300 \text{ }^\circ\text{C}$ , and gas flow rates of 1960, 80, and  $50 \text{ cm}^3/\text{min}$  for  $\text{N}_2$ ,  $\text{SiH}_4$ , and  $\text{NH}_3$  respectively. AZ 5214-E was used as positive tone photoresist (PR) for photolithography and was spun coat on  $\text{Si}_3\text{N}_4$  at 4000 rpm for 45 s. Following prebake at  $110 \text{ }^\circ\text{C}$  for 60 s to remove moisture, PR was exposed to UV ( $\lambda = 405 \text{ nm}$ ) radiation at  $21.6 \text{ mW}/\text{cm}^2$  for 9.6 s through a chrome mask. Then PR was developed in AZ 327 MIF (metal ion free) for 32 s followed by treatment with oxygen plasma (Jupiter III, March Instruments) at 600 mTorr under 100 W for 3 min. After hard bake at  $120 \text{ }^\circ\text{C}$  for 2 min, the  $\text{Si}_3\text{N}_4$  layer was then etched using  $\text{CF}_4$  reactive ion etching (Freon/ $\text{O}_2$  RIE, PlasmaLab) at a pressure of 35 mTorr under 90 W for 5.3 min to achieve an etch depth of  $\sim 300 \text{ nm}$ . Finally, residual PR was removed using acetone in an ultrasonic bath for 5 min followed by piranha cleaning ( $\text{H}_2\text{SO}_4:\text{H}_2\text{O} = 3:1$ ) for 2 min. The fabricated structures are shown in the optical image (Fig. 3(a)) and scanning electron microscopy (SEM) top view image (top right inset of Fig. 3(a)). The cross-sectional height profiles of the fabricated GFRs were analyzed with an atomic force microscope (AFM) (Dimension 3000, Digital Instruments) in tapping mode using a monolithic silicon tip with 30-nm-thick aluminum reflex coating (Budget Sensors), as shown in Fig. 3(b). Based on AFM measurements the structure parameters  $\Lambda$ ,  $f$ ,  $\theta_1$ ,  $\theta_2$ , and  $d_1$  of the fabricated GFRs were evaluated (Table 1). In addition, each structure is resonant with two orthogonal polarizations of incident light, enabling TE and TM modes of each structure to double the number of available filter wavelengths.

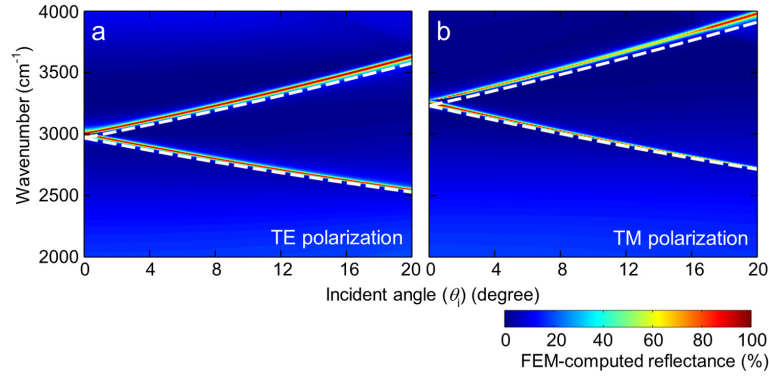


Fig. 2. Spectral response of the GFR as a function of incident angle ( $\theta$ ) and wavenumber for (a) TE polarization and (b) TM polarization. Far-field reflectance is computed using FEM for a GFR structure with  $[\Lambda, \theta_1, \theta_2, f, d_2, d_1] = [2 \mu\text{m}, 55^\circ, 55^\circ, 0.35, 580 \text{ nm}, 300 \text{ nm}]$ . Analytically predicted resonance peaks (white dashes) based on Eq. (1) and the calculated dispersion curves for  $t_{\text{slab}} = 730 \text{ nm}$  in Fig. 1(d) are overlaid for comparison. Refractive indices  $n_{\text{SiN}} = 2.02$  and  $n_{\text{SL}} = 1.47$  are assumed in both FEM computation and analytical prediction.

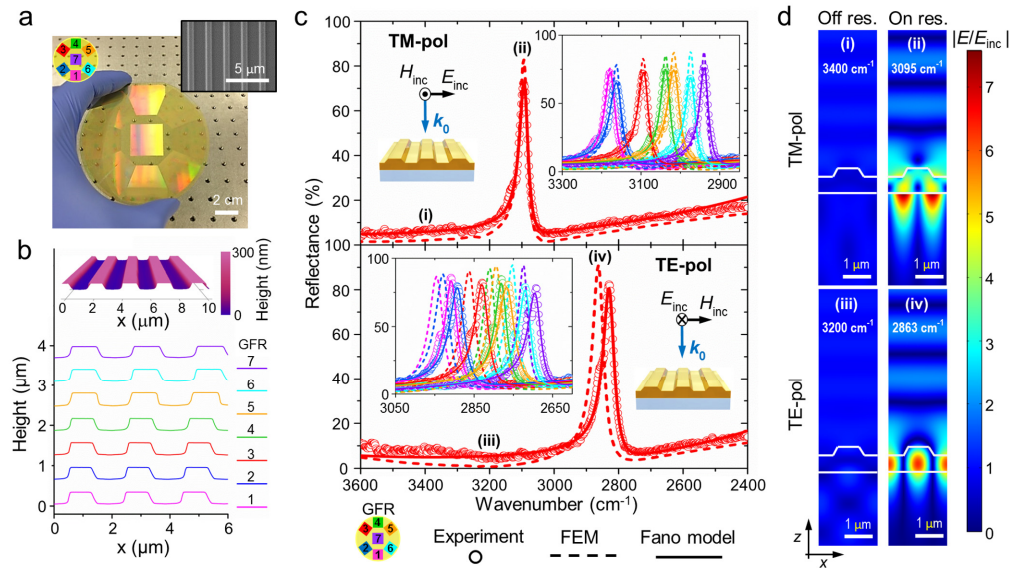


Fig. 3. Large-area mid-IR GFRs with narrow bandwidth and high CR. (a) Optical image of a set of large-area GFRs built on a 4-inch soda lime glass substrate. Top right inset: SEM image of a fabricated structure. (b) AFM cross-sectional profiles, vertically offset for clarity. The 3-D AFM topography image of the structure 7 (GFR-7) is shown in the top inset. (c) Measured and FEM-computed far-field reflectance spectra of a representative device (GFR-3) when a TM-polarized (top) or TE-polarized (bottom) light is normally incident, along with the zoomed-in spectra in the vicinity of the resonances of all GFRs as shown in the inset. Each experimental spectrum is also fitted with the Fano interference model (Eq. (2)). (d) FEM-computed electric field amplitude ( $|E/E_{\text{inc}}|$ ) distributions in a unit cell of the GFR-3 at the indicated spectral locations in (c).

**Table 1. Structural parameters of the fabricated GFRs**

GFR structure	$\Lambda$ [ $\mu\text{m}$ ]	$d_1$ [nm] <sup>a</sup>	$f$ [%]	$\theta_1$ [°]	$\theta_2$ [°]	$d_2$ [nm] <sup>a</sup>
1	2.0371	290.7	33.5	57.8	48.7	580
2	2.0715	293.6	31.9	57.3	48.4	542
3	2.1029	301.1	34.4	61.7	54.7	585
4	2.1294	295.3	36.1	58.1	54.2	622
5	2.1574	323.3	37.9	60.1	64.1	593
6	2.2069	304.5	34.4	57.7	48.9	580
7	2.2470	277.1	36.1	54.5	49.2	568

<sup>a</sup>Fabrication uniformity of the large-area device can be estimated by evaluating  $\langle d_1 \rangle = 297.94$  nm,  $\sigma(d_1) = 13.14$  nm, and  $\sigma(d_1)/\langle d_1 \rangle = 4.41\%$   
 $\langle d_2 \rangle = 581.43$  nm,  $\sigma(d_2) = 22.46$  nm, and  $\sigma(d_2)/\langle d_2 \rangle = 3.86\%$   
 $\langle t_{\text{slab}} \rangle = \langle d_2 + 0.5d_1 \rangle = 730.40$  nm,  $\sigma(t_{\text{slab}}) = 25.31$  nm, and  $\sigma(t_{\text{slab}})/\langle t_{\text{slab}} \rangle = 3.46\%$   
where  $\langle \dots \rangle$  and  $\sigma(\dots)$  denote mean average and standard deviation, respectively.

Figure 3(c) shows the measured and calculated far-field reflectance at normal incidence for a representative resonator (GFR-3) along with the zoomed-in spectra in the vicinity of resonances for all GFRs. Far-field spectra were measured by using a Fourier-transform spectrometer (Vertex 70, Bruker), and reflectance values were evaluated by normalizing the spectral response of a GFR to that of a gold mirror. Two complementary approaches were pursued here to model the measured results. FEM simulations are used to compute the far-field reflectance spectra and the near-field electric field amplitude ( $|E/E_{\text{inc}}|$ ) distribution of the GFRs. Dispersion and optical absorption of the materials [60, 61] and structural parameters extracted from AFM measurements (Table 1) were used in the FEM computation in Fig. 3(c). Here we used FEM to ‘fit’ our measured reflection spectra data, and  $d_2$  was the only fit parameter. A proper value of  $d_2$ , as listed in Table 1, was obtained for each structure by matching the resonance wavenumber in the FEM-computed TM-polarized spectrum to the experimental value. To explain the lineshape of the resonance as the result of Fano interference effect, experimental reflection spectra are fitted to Eq. (2). The resonance bandwidth, lineshape of resonance, and off-resonance reflectance in the measured far-field reflection spectra closely match FEM predictions.

The off-resonance background reflectance in Fig. 3(c) originates from continuum F–P multiple reflections, as described in the Fano interference model (Eq. (2)). The fabricated narrowband GFRs here have a corresponding  $t_{\text{slab}}$  of  $\sim 730$  nm (Table 1), and exhibit a minimum continuum reflectance of  $\leq 10\%$  at  $2800\text{--}3300$   $\text{cm}^{-1}$  in the experimental spectra, showing good agreement with the theoretical predictions of  $R_{\text{F-P}}$  presented in Fig. 1(c) for an equivalent flat thin-film slab. As a result, the off-resonance background in the measured reflectivity spectra of GFRs is increased outside this spectral range. The width of this low-background spectral range can be enlarged and the background reflection can be further suppressed by incorporating additional layers for broadband antireflection coating [62].

Because of high  $R_{\text{peak}}$  at resonance, the interference of the downward incident wave and upward reflected wave at resonance creates obvious standing wave patterns along the  $z$  direction in air, as seen in the near-field  $|E/E_{\text{inc}}|$  distribution in Fig. 3(d). The on-resonance  $|E/E_{\text{inc}}|$  distribution for TE polarization shows two maxima per unit cell within the slab in the in-plane ( $x$ ) direction due to interference of guided waves propagating in opposite ( $\pm x$ )

directions, confirming the momentum-matching condition (that is,  $|k_{\text{model}}| = 2\pi/\Lambda$  at resonance) [63]. Combining both high  $R_{\text{peak}}$  and low  $R_{\text{vicinity}}$  of  $\sim 5\text{--}8\%$ , our one-layer resonant filters possess a  $CR$  (listed in Table 2) of 9.8–13.7 and 9.4–14.8 for TM and TE polarization respectively, showing  $>200\%$  increase of  $CR$  than devices reported previously [64] (as seen in Fig. 4). Additionally, it is interesting to note that the very simple GFRs here show  $\lambda_{\text{peak}}/\Delta\lambda$  and  $CR$  values comparable to that of recently developed narrowband mid-IR thermal emitters, based on rod-type two-dimensional PC structures comprising 13 pairs of quantum-well epitaxial layers [65], which are much more complicated. The measured far-field reflectance spectra of the fabricated GFRs and the fit with the Fano interference model match very well, from which values for  $\{v_{\text{res}}, \Delta\nu, Q, P_r/P_c, \phi\}$  are determined and listed in Table 2. For guided Fano resonance, the phase difference ( $\phi$ ) goes to zero and the lineshape becomes symmetric when the direct F–P reflectivity reaches minimum [49, 66]. Our GFRs here are designed to have low F–P background; consequently,  $\phi$  is small for fabricated resonators.

**Table 2. Value of resonance wavenumbers ( $v_{\text{res}}$ ), linewidth ( $\Delta\nu$ ), quality factor ( $Q$ ), ratio of the powers in the Lorentzian resonance to in the direct continuum background ( $P_r/P_c$ ), the relative phase difference between these two channels ( $\phi$ ), and contrast ratio ( $CR$ ) by a fit with Eq. (2) of the experimental spectra in Fig. 3(c)**

	GFR	$v_{\text{res}}$ [cm <sup>-1</sup> ]	$\Delta\nu$ [cm <sup>-1</sup> ]	$Q^a$	$P_r/P_c$	$\phi$ [rad.]	$CR^b$
TM-pol	1	3176.5	32.2	99	7.8	-0.58	14.8
	2	3159.8	37.6	84	5.3	-0.74	10.7
	3	3090.9	32.1	96	5.8	-0.76	11.6
	4	3035.6	30.3	100	6.6	-0.65	11.2
	5	3014.4	37.5	80	5.6	-0.63	11.3
	6	2971.7	30.0	99	6.2	-0.73	10.2
	7	2937.4	27.5	107	6.4	-0.71	9.4
TE-pol	1	2906.1	38.6	75	8.3	-0.58	13.7
	2	2889.6	44.9	64	5.7	-0.69	9.8
	3	2826.9	41.7	68	6.3	-0.74	10.5
	4	2778.2	36.6	76	5.8	-0.69	11.9
	5	2763.7	50.2	55	5.9	-0.66	10.6
	6	2716.4	37.5	72	5.4	-0.84	11.1
	7	2691.8	39.3	68	4.7	-0.83	11.6

<sup>a</sup> $Q = v_{\text{res}}/\Delta\nu \cong \lambda_{\text{peak}}/\Delta\lambda$ ; <sup>b</sup> $CR = R_{\text{peak}}/R_{\text{vicinity}}$ , where  $R_{\text{vicinity}} = |a_c(v_{\text{res}})|^2$  is estimated by fitting experimental spectra to Eq. (2).

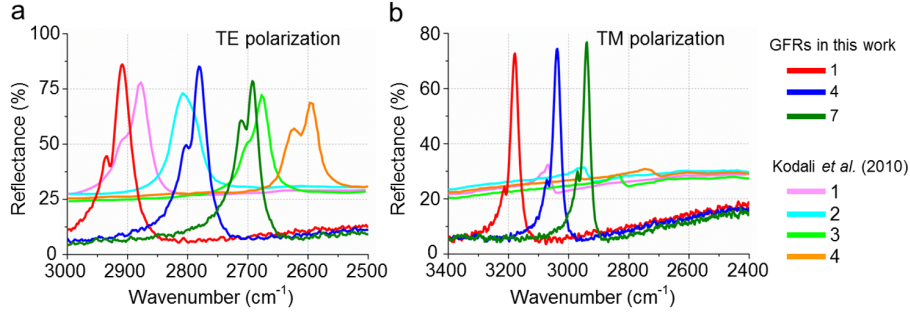


Fig. 4. Comparison of measured spectra of the GFRs in the present work and the devices reported previously [64] for (a) TE polarization and (b) TM polarization. (Reproduced with permission from [64]. Copyright 2010 American Chemical Society.)

### 2.3. A GFR-based instrument and DF-IR spectroscopic imaging

Figure 5(a) schematically illustrates the GFR-based instrument constructed for DF-IR imaging. Broadband IR emission from a SiC incandescent source is collimated by an off-axis parabolic mirror. Two circular apertures used to filter divergent IR radiations reduce the optical beam diameter to  $\sim 17$  mm. Polarization of the beam is controlled by a wire-grid polarizer. Narrowband IR beam reflected by a GFR is directed toward the microscope by a beam splitter. After the beam enters the microscope, it is condensed through an IR aspheric lens (NT68-245, Edmund Optics) with a NA of 0.63 before passing through the sample, and then the transmitted beam is collected by an objective lens (#390028, LightPath) with a NA of 0.56. Images are captured by a liquid-nitrogen-cooled mercury cadmium telluride (MCT)  $128 \times 128$  pixel focal plane array (FPA) detector (SBF161, Santa Barbara Focalplane) with a wide detection range ( $\nu = 1000\text{--}5000$   $\text{cm}^{-1}$  or  $\lambda = 2\text{--}10$   $\mu\text{m}$ ). Given the large spectral range compared to other forms of spectroscopy, a major challenge is that even small out-of-band contributions can overwhelm in-band signals. A broadband pass filter (BBP-3000-3900c nm, Spectrogon) is employed to reject IR radiation outside  $2500\text{--}3300$   $\text{cm}^{-1}$  ( $\lambda = 3.3\text{--}4.0$   $\mu\text{m}$ ). Both the GFR wheel mounting stage and the sample stage are motorized and controlled by a personal computer. Figure 5(b) shows measured spectral densities [67] of the broadband incandescent IR source and the GFR-reflected narrow-bandwidth IR beam. Rotating the motorized mounting stage brings a specific GFR into the beam path, enabling rapid wavelength tuning. The DF-IR absorbance ( $A_{\text{DF-IR}}$ ) at any discrete frequency ( $\nu_{\text{res}}$  of the GFR) using a GFR filter is evaluated as

$$A_{\text{DF-IR}} \Big|_{\nu=\nu_{\text{res}}} = \log_{10} \left( \frac{I_{\text{ref}} - I_{\text{db}}}{I_{\text{sample}} - I_{\text{db}}} \right) \quad (4)$$

where  $I_{\text{sample}}$  is the transmitted IR intensity through the sample,  $I_{\text{ref}}$  is the reference IR intensity through the unmodified IR-transparent substrate, and  $I_{\text{db}}$  is the dark-background IR intensity due to ambient radiation when the input port of the microscope is closed.

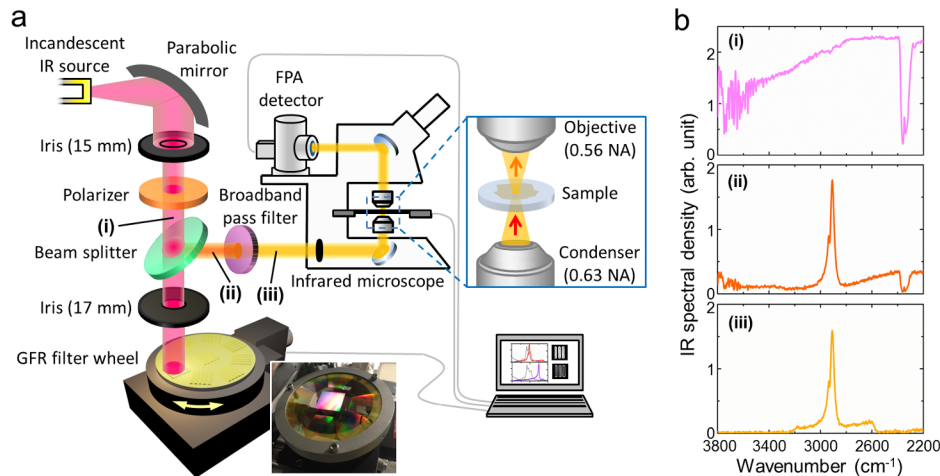


Fig. 5. (a) Schematic of GFR-based DF-IR spectroscopic imaging microscopy. Bottom inset: motorized GFR wheel mounting stage. Right inset: narrowband IR radiation passes through a sample under test. NA, numerical aperture. (b) IR spectra at the indicated beam locations in (a).

Until now, there has not been a report of spectroscopic imaging using Fano-type narrowband radiation in the mid-IR. Hence, we validate our microscopy setup with a SU-8 polymer USAF target. The USAF resolution target is made of a patterned layer ( $\sim 10 \mu\text{m}$  thick) of SU-8 polymer (MicroChem) on a polished barium fluoride ( $\text{BaF}_2$ ) substrate (ISP Optics), fabricated using the conventional protocol of photolithography.

Although SU-8 is transparent in the visible region of the spectrum, as seen in the optical image in Fig. 6(a), it contains distinctive absorption bands in the C–H stretching region. As shown in Fig. 6(b), DF-IR absorbance images clearly demonstrate the spatial fidelity and spectral content of the target. The  $\text{BaF}_2$  area has  $A_{\text{DF-IR}} \approx 0$  because it is IR transparent. In addition to ‘Absorption ON/OFF’ imaging, it is also interesting to investigate DF-IR absorbance as a function of discrete wavelengths. Figure 6(c) shows a series of DF-IR absorbance images and their corresponding spectra using a set of GFRs. The spectral densities of the GFR-reflected IR beam (colored in Fig. 6(c)) were characterized by coupling the beam to a Bruker Vertex 70 spectrometer. The IR absorbance spectra of the SU-8 resolution target (grey in Fig. 6(c)) were measured with a FT-IR imaging microspectrometer (620-IR, Varian) equipped with a MCT FPA detector and a  $15 \times$  Schwarzschild objective and condenser with a NA of 0.4 to provide IR spectral images with a  $\sim 725 \mu\text{m}$  field of view and a spatial resolution of ca.  $5.65 \mu\text{m} \times 5.65 \mu\text{m}$ . The FT-IR absorbance values ( $A_{\text{FT-IR}}$ ) were evaluated by converting the ratio of single beam spectra to an appropriately acquired reference spectrum using Beer-Lambert law. As seen in Fig. 6(c), the DF-IR absorbance of the three SU-8 bars gradually gets higher/lower when the peak of the GFR-reflected IR beam enters/exits the IR absorption bands of SU-8. Figure 6(d) shows the absorbance spectrum measured by DF-IR imaging, compared to a corresponding FT-IR measurement. The data agree reasonably with the discrepancy arising from the Fano lineshape, the finite linewidth, and background reflectance of the GFRs and differences in optical setup between the two systems [68, 69].

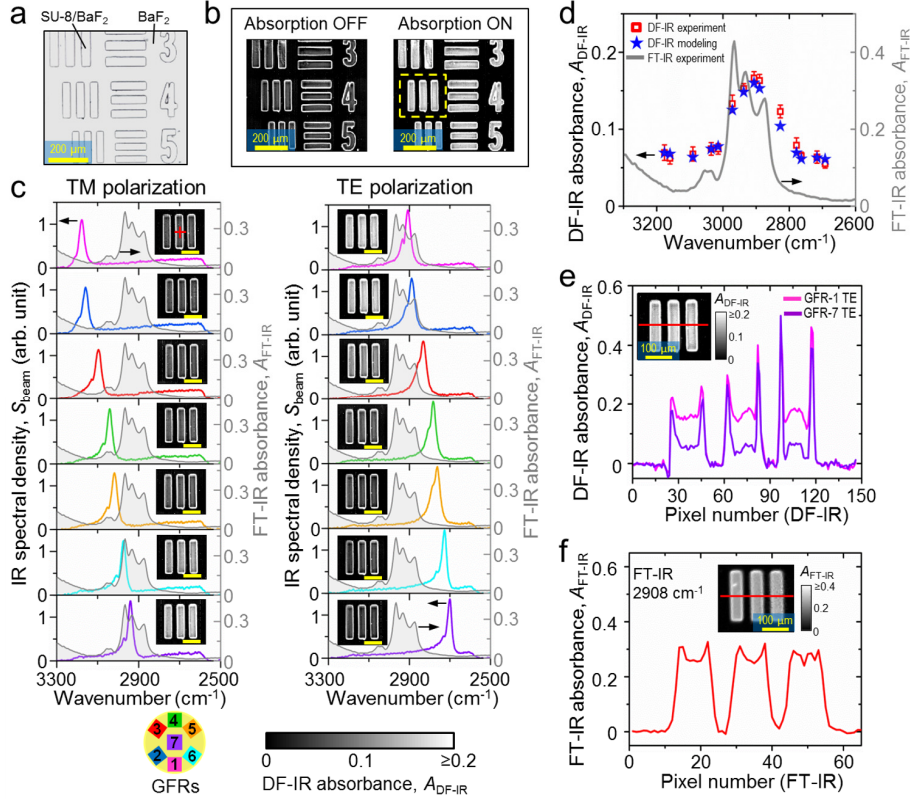


Fig. 6. DF-IR spectroscopic imaging of a USAF resolution target made of SU-8 polymer. Optical microscopic image (a) and mosaic DF-IR absorbance images (b) of a USAF resolution target (group 3, element 3, 4, and 5) when the resonance of the GFRs is outside (*left*, using TE-polarized GFR-6) or within (*right*, using TE-polarized GFR-1) the IR absorption bands of SU-8 polymer. (c) A series of DF-IR absorbance images of the area defined by the yellow dashed square in (b) using a set of GFRs made and their corresponding spectra (colored: measured IR spectral density of the beam before entering the microscope; grey: measured FT-IR absorbance spectra of SU-8 polymer at the position denoted by the red cross in the top left inset of (c)). Scale bar 100  $\mu\text{m}$ . (d) Measured (averaged over  $3 \times 3$  pixels, with error bars indicating  $\pm 1$  standard deviation,  $N = 9$ ) and calculated DF-IR absorbance spectra of SU-8 polymer at the location denoted by the red cross in the top left inset of (c), along with the measured FT-IR absorbance spectrum at the same place. Fitted resonance wavenumbers in Table 2 were used to determine the spectral positions of DF-IR data set. (e) Measured DF-IR absorbance profiles along the red line in the inset. The DF-IR image in the inset is the same as for TE-polarized GFR-1 shown in (c). (f) Measured FT-IR absorbance image of the same area and FT-IR absorbance profile along the red line at  $2908 \text{ cm}^{-1}$ , which is close to the resonance wavenumber of the TE-polarized GFR-1.

To address the discrepancy due to GFR characteristics, we developed a simple model to quantitatively explain the DF-IR spectrum. Based on Eq. (4), the modeled DF-IR absorbance can be written as

$$A_{\text{DF-IR}} \Big|_{\text{at peak wavenumber}} = \log_{10} \left( \frac{\int S_{\text{beam}}(\nu) T_{\text{cond}}(\nu) T_{\text{obj}}(\nu) d\nu}{\int S_{\text{beam}}(\nu) T_{\text{cond}}(\nu) T_{\text{obj}}(\nu) 10^{-A_{\text{FT-IR}}(\nu)} d\nu} \right) \quad (5)$$

where  $S_{\text{beam}}(\nu)$  represents the measured spectral density of the narrowband IR beam (colored in Fig. 6(c)), and  $A_{\text{FT-IR}}(\nu)$  represents a measured FT-IR absorption spectrum (grey in Fig. 6(c) and 6(d)).  $T_{\text{cond}}(\nu)$  and  $T_{\text{obj}}(\nu)$  are the transmittance spectra of the condenser and the objective lens, respectively (see Fig. 7). The integrations in the denominator and the numerator

represent the transmission IR intensity through a thin layer of sample and the reference IR intensity through the air, respectively. As shown in Fig. 6(d), the measured and modeled DF-IR absorbance spectra match very well. Therefore, the DF-IR system and its performance can be predicted, analyzed, and understood.

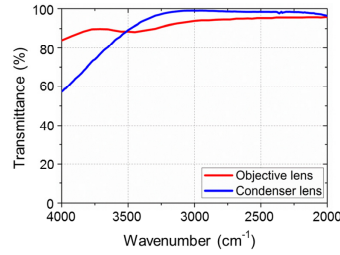


Fig. 7. Transmittance spectra of the objective lens (LightPath) and condenser lens (Edmund Optics).

For QCL-based IR spectral imaging [19],  $S_{\text{beam}}(\nu)$  has a delta-function-like spectrum, and therefore according to Eq. (5) we have  $A_{\text{DF-IR}} \approx A_{\text{FT-IR}}$  and imaging with high spectral sensitivity. For GFR-based IR spectral imaging,  $S_{\text{beam}}(\nu)$  has a finite linewidth  $\Delta\nu$  (due to coupling of the resonant guided mode to radiation channels outside the GFR) and background intensity (due to continuum F-P reflection of GFRs and the broadband incandescent IR source used), as shown in Fig. 6(c). Accordingly,  $A_{\text{DF-IR}}$  is an average absorbance weighted by the Fano-like spectrum of  $S_{\text{beam}}(\nu)$  according to Eq. (5), leading to  $A_{\text{DF-IR}} \leq A_{\text{FT-IR}}$  when  $\nu_{\text{res}}$  is within the IR absorption bands of the sample ('Absorption ON' state) and  $A_{\text{DF-IR}} \geq A_{\text{FT-IR}}$  when  $\nu_{\text{res}}$  is outside the IR absorption bands ('Absorption OFF' state), respectively. As a result, the DF-IR spectrum here shows a spectral sensitivity less than the FT-IR counterpart, with the peak  $A_{\text{DF-IR}}$  value  $\sim 2$  times larger than the 'Absorption OFF'  $A_{\text{DF-IR}}$  as shown in Fig. 6(d). Despite of this fact, engineering of narrow-bandwidth GFRs for low background reflectance and high  $CR$  in the vicinity of the spectral range of interest (Section 2.1 and 2.2) is the key to successfully observing the DF-IR spectroscopic contrast here that cannot be seen if using the devices reported previously (Fig. 4). The spectral sensitivity of the GFR-based DF-IR can be further enhanced by using narrowband multilayered GFRs with wideband antireflection design.

In addition to comparisons of the DF-IR and FT-IR spectra, the DF-IR absorbance spatial profiles of the three SU-8 bars (Fig. 6(e)) are compared to the case measured with a FT-IR imaging microspectrometer (Fig. 6(f)). The height of profiles reflects value of the local DF-IR absorbance, and the sudden increase of absorbance at the edges is due to light scattering [19, 70], which is more apparent in DF-IR measurement due to the higher NA used. It is notable that in contrast to the QCL-based IR imaging system [19] where spatial coherence of laser introduces undesired fringe patterns into microscopic images, the GFR-based DF-IR instrument described here shows imaging quality comparable to that of the conventional FT-IR imaging.

The GFR-enabled DF-IR instrument also allows for the investigation of the IR absorption spectra of biological specimens. Figure 8(a) shows the optical image of an unstained human breast tissue sample (US Biomax), with a zoomed-in area of epithelium shown in the right inset. Breast tissue consists of complex microstructures which may have dissimilar IR response for different optical polarizations. In order to focus on the optical absorption and not on polarization, here we probed DF-IR absorbance of tissue using narrowband IR beam with the same polarization (TM) reflected by the GFR wheel. Figure 8(b) shows measured DF-IR and FT-IR absorbance spectra at the indicated location in Fig. 8(a), along with the corresponding  $S_{\text{beam}}(\nu)$  spectra for GFRs used. The trend of the DF-IR absorbance spectrum of breast tissue matches that of the FT-IR spectrum. In the top inset of Fig. 8(b), the FT-IR image at  $2938 \text{ cm}^{-1}$  (corresponding to  $\nu_{\text{res}}$  of GFR-7) shows generally higher absorbance than the FT-IR image at  $3014 \text{ cm}^{-1}$  (corresponding to  $\nu_{\text{res}}$  of GFR-5). In comparing DF-IR images

as shown in Fig. 8(c), we observe that the same contrast can be seen in DF-IR images that is observed in FT-IR imaging data as shown in Fig. 8(b). Notably, we see that the epithelium can be readily discernible with just one frequency. Of course, use of other frequencies and spectral features can be used to refine this visualization and provide complete histopathological imaging.

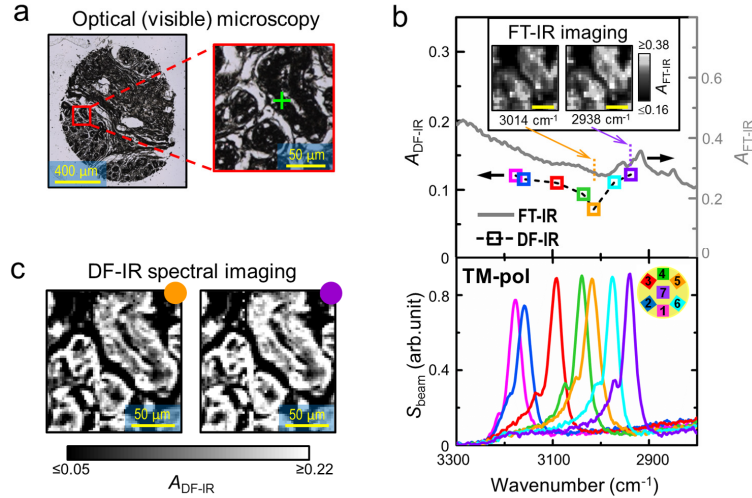


Fig. 8. DF-IR spectral imaging of human breast tissue. (a) Optical images of an unstained human breast tissue specimen. (b) DF-IR absorbance spectrum (top) at the location marked by the green cross in (a) probed by narrowband IR beam reflected by the TM-polarized GFR wheel (IR spectral density  $S_{\text{beam}}(\nu)$  shown in the bottom). FT-IR absorbance spectrum at the same location and FT-IR absorbance images of the area defined by the red square in (a) at  $2938 \text{ cm}^{-1}$  and  $3014 \text{ cm}^{-1}$  (corresponding to  $\nu_{\text{res}}$  of TM-polarized GFR-7 and GFR-5, respectively) are also provided in the top for reference. Scale bar  $50 \mu\text{m}$ . (c) DF-IR absorbance imaging, showing higher absorbance of tissue for GFR-7 (purple) than the value for GFR-5 (orange).

### 3. Conclusion

By fully grasping the underlying principle and carefully designing, we sculpted optical properties of mid-IR GFRs for narrow bandwidth and high  $CR$ , which showed of critical importance in DF-IR spectroscopic measurements. The collective set of results indicates that the concept and method of the DF-IR spectroscopic imaging can be applied not only to study of condensed matter materials but also to biological applications. While different type of tissue cells have similar mid-IR absorption spectra in the C–H stretching region, they show dissimilar spectral features in the fingerprint mid-IR region ( $1000\text{--}1600 \text{ cm}^{-1}$ ), where optimal discrete spectral regions have been discovered for automated cancer pathology [13, 71]. Therefore, once an appropriate set of narrowband high- $CR$  GFRs at those characteristic wavelengths are made, IR cancer pathology will benefit from efficiency and robust instrumentation of the GFR-based DF-IR technology. Looking forward, in conjunction with development of high-performance IR photodetectors and GFRs in other regions of the mid-IR spectrum, GFR-based DF-IR technology opens a number of new opportunities for mid-IR spectroscopy. In addition to efficient spectral imaging, GFR-based DF-IR technology could also make video-rate imaging measurements possible for a variety of applications.

### Appendix A. Computation of Fabry–Pérot reflectance of a flat thin-film slab

By using the propagation matrix approach [58, 59] the incident, reflected, and transmitted waves are related in a dielectric slab with a thickness  $t_{\text{slab}}$  as depicted in the bottom left inset of Fig. 1(c):

$$\begin{bmatrix} E_0 \\ rE_0 \end{bmatrix} = \mathbf{B} \begin{bmatrix} tE_0 \\ 0 \end{bmatrix} \quad (6)$$

where  $E_0$  is the amplitude of the incident wave, and  $r$  and  $t$  are the reflection and transmission coefficients, respectively. The backward-propagation matrix  $\mathbf{B}$  is defined as

$$\begin{aligned} \mathbf{B} &= \frac{1}{2} \begin{bmatrix} (1 + P_{\text{air}|\text{SiN}}) e^{-ik_{z,\text{SiN}} t_{\text{slab}}} & (1 - P_{\text{air}|\text{SiN}}) e^{ik_{z,\text{SiN}} t_{\text{slab}}} \\ (1 - P_{\text{air}|\text{SiN}}) e^{-ik_{z,\text{SiN}} t_{\text{slab}}} & (1 + P_{\text{air}|\text{SiN}}) e^{ik_{z,\text{SiN}} t_{\text{slab}}} \end{bmatrix} \frac{1}{2} \begin{bmatrix} (1 + P_{\text{SiN}|\text{SL}}) & (1 - P_{\text{SiN}|\text{SL}}) \\ (1 - P_{\text{SiN}|\text{SL}}) & (1 + P_{\text{SiN}|\text{SL}}) \end{bmatrix} \\ &= \begin{bmatrix} b_{11} & b_{12} \\ b_{21} & b_{22} \end{bmatrix} \end{aligned} \quad (7)$$

where  $P_{\text{air}|\text{SiN}} = n_{\text{SiN}}/n_{\text{air}}$ ,  $P_{\text{SiN}|\text{SL}} = n_{\text{SL}}/n_{\text{SiN}}$ , and  $k_{z,\text{SiN}} = k_0 n_{\text{SiN}} = (2\pi/\lambda) n_{\text{SiN}}$  for normal incidence ( $\theta_i = 0^\circ$ ). In our case, all of the materials are dielectric and non-magnetic (relative permeability of the medium  $\mu_r = 1$ ). The F-P reflectance is obtained by

$$R_{\text{F-P}} = |r|^2 = \left| \frac{b_{21}}{b_{11}} \right|^2 \quad (8)$$

The method shown here can be easily generalized to multilayered optical thin-film structures.

### Appendix B. Dispersion and cutoff of guided modes

By using the dielectric waveguide theory [59], the propagation wavevector  $k_{\text{mode}}$  can be obtained by solving the eigenequations for guidance condition for a guided mode with a mode number  $m$  in a dielectric slab with a thickness  $t_{\text{slab}}$ :

$$\sqrt{(n_{\text{SiN}} k_0)^2 - k_{\text{mode}}^2} t_{\text{slab}} = \tan^{-1} \left( \frac{\alpha_{\text{air}}}{\sqrt{(n_{\text{SiN}} k_0)^2 - k_{\text{mode}}^2}} \right) + \tan^{-1} \left( \frac{\alpha_{\text{SL}}}{\sqrt{(n_{\text{SiN}} k_0)^2 - k_{\text{mode}}^2}} \right) + m\pi \quad (9)$$

for the  $\text{TE}_m$  mode, and

$$\sqrt{(n_{\text{SiN}} k_0)^2 - k_{\text{mode}}^2} t_{\text{slab}} = \tan^{-1} \left( \frac{n_{\text{SiN}}^2}{n_{\text{air}}^2} \frac{\alpha_{\text{air}}}{\sqrt{(n_{\text{SiN}} k_0)^2 - k_{\text{mode}}^2}} \right) + \tan^{-1} \left( \frac{n_{\text{SiN}}^2}{n_{\text{SL}}^2} \frac{\alpha_{\text{SL}}}{\sqrt{(n_{\text{SiN}} k_0)^2 - k_{\text{mode}}^2}} \right) + m\pi \quad (10)$$

for the  $\text{TM}_m$  mode;  $\alpha_{\text{air}}$  and  $\alpha_{\text{SL}}$  are the decay constants in the transverse ( $z$ ) direction in air and in the soda lime substrate, respectively, and are defined as

$$\alpha_{\text{air}} = \sqrt{k_{\text{mode}}^2 - (n_{\text{air}} k_0)^2} \quad (11)$$

$$\alpha_{\text{SL}} = \sqrt{k_{\text{mode}}^2 - (n_{\text{SL}} k_0)^2} \quad (12)$$

When cutoff, decay constant vanishes in the substrate region, leading to  $\alpha_{\text{SL}} = 0$  and  $k_{\text{mode}} = k_0 n_{\text{SL}}$ . Then the cutoffs can be determined from Eq. (9) and (10).

### Acknowledgments

This work was supported by a grant from the National Institutes of Health (grant number R01 EB009745A). J.N.L. acknowledges the support of Taiwan's Government Fellowship for Studying Abroad. M.V.S. thanks support through the Congressionally Directed Medical Research Program Postdoctoral Fellowship BC101112.